Research Article

Preparation, structural and spectroscopic study of sol-gel-synthesized Cr^{3+}:Al_2O_3 powder

Otávio A. Capeloto[1] · Nivaldo E. de Souza[2] · Ivair A. Santos[1] · Nelson G. C. Astrath[1] · Isabella. T. P. Miranda[3] · Luiz A. Pilatti[3] · Ana A. W. Hechenleitner[4] · Edgardo A. G. Pineda[4] · Maurício A. C. de Melo[1]

Received: 25 July 2019 / Accepted: 3 November 2019 / Published online: 12 November 2019

Abstract

Chromium-doped α-Al_2O_3 powder was synthesized by a modified sol–gel method using poly(vinyl alcohol) aqueous solutions and metal nitrate precursors. The synthesis process is simple, is of low cost and produced final crystals with cubic shape as confirmed by X-ray diffraction. The morphology of the samples verified by scanning electron microscopy showed slabs with thickness below 1 µm, formed by interconnected long grains of typical thickness of around 200 nm, showing growth of the grains as followed by thermogravimetric analysis. Luminescence characteristics of Cr^{3+}were detected and analyzed as a function of the concentration of chromium using photoacoustic and photoluminescence spectroscopies.

Graphic abstract

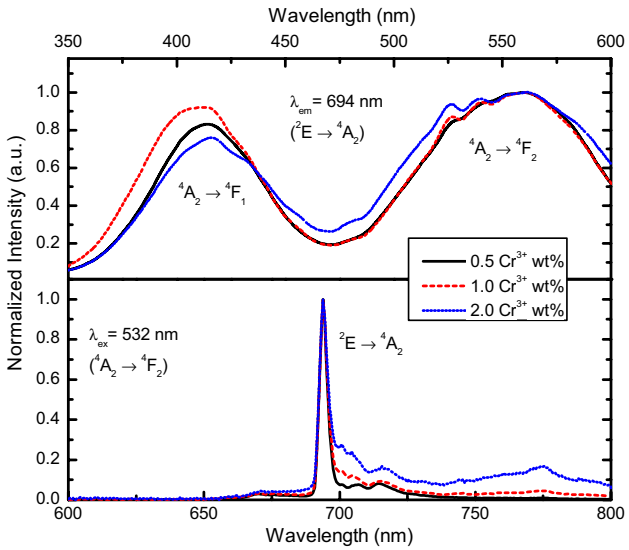

Keywords Characterization · Luminescence · Nanostructure · Optical property · Powder synthesis · Sol–gel

✉ Otávio A. Capeloto, oacapeloto@gmail.com | [1]Departamento de Física, Universidade Estadual de Maringá, Maringá, PR 87020-900, Brazil. [2]Instituto Federal do Paraná (IFPR), Câmpus Paranavaí, Paranavaí, PR 87703-536, Brazil. [3]Programa de Pós-Graduação em Engenharia de Produção (PPGEP), Universidade Tecnológica Federal do Paraná (UTFPR), Câmpus Ponta Grossa, Ponta Grossa, PR 84016-210, Brazil. [4]Departamento de Química, Universidade Estadual de Maringá, Maringá, PR 87020-900, Brazil.

SN Applied Sciences (2019) 1:1597 | https://doi.org/10.1007/s42452-019-1631-9

1 Introduction

Luminescent materials play an important role in facing new technologies, specially those used in lighting, displays, solar cells, scintillator and sensors, in general [1, 2]. In solar cells, for example, a luminescent material is used to convert ultraviolet/infrared into visible light by down-/up-conversion fluorescence mechanisms. The enhanced visible light is then absorbed by the semiconducting material used to produce solar cells [2].

Optical amplification using luminescent materials has been reported as useful for many applications [3–7]. In many cases, erbium- or bismuth-doped glasses are pumped at selected wavelengths for obtaining emissions at 1.3 μm and 1.55 μm. Such amplification at this spectral region is useful for optical communications due to the low dispersion in low-loss silica fibers [3–5], for instance. As different wavelengths may affect directly human health [8, 9], the search for an ideal light lamp is supported by different kinds of luminescent materials to produce many combinations of different wavelengths [10]. Usually, an emitting phosphor is placed within the light bulb, which converts electric energy into UV radiation, exciting the emitting phosphor, inducing the production of visible light. White light LEDs are commonly produced using yellow, green or red dyes excited by a blue-emitting LED source [10].

Another important application of luminescent materials is for cooling down surfaces by coating it with luminescent materials. The reflectance of the coating and further conversion of sunlight photons into light emission due to luminescence processes decrease the heat generated by the luminous energy impinged on the surface by the sun. Practical applications in urban structures and buildings can affect directly life quality of people, reducing internal temperature of environments, increasing the comfort and decreasing the electric energy consumed due the cooling machines [11–14]. An example of such kind of luminescent material is ruby, as reported recently by Berdahl et al. [15].

Ruby (Cr^{3+}:Al_2O_3) crystals are well-characterized luminescent materials [15–22], with applications as active medium for solid-state laser, since pioneer studies reported by Maiman [16, 17]. Ruby is also employed into diamond anvil cells using the pressure sensitive R_1 emission line of ruby to measure the applied pressure on the samples by detecting its fluorescence shift [23, 24].

Ruby powder is typically obtained by the conventional solid-state reaction [25–27]. To attain wanted phase purity, the solid-state reaction process takes up to 10 h at 1200 °C treatment and up to 6 h in ball mill mixing [26], which might introduce further impurities and defects to the end product. In addition, due to high-temperature treatment, the stoichiometry of the inertial reagents cannot be well controlled.

Wet chemical route generally is a good way to resolve it [28]. The fine control of the stoichiometry of metals and high homogeneity of end products can be provided by wet chemical synthesis routes [29–33]. The stoichiometry control is attributed to the mixing of starting materials at the molecular level. Furthermore, there is a significant decrease in the synthesis temperatures and also in the time of thermal treatment in comparison with the solid-state reaction method. Besides that, the small size powders with foreseeable morphology could be obtained by the sol–gel method. Nanosized powders can later facilitate the attainment of high-density ceramics. However, sometimes wet chemical synthesis routes become quite complicated with the use of numerous reagents.

Here, we use a simple sol–gel modified method using water as a solvent to prepare ruby (Cr^{3+}:Al_2O_3) powders with different concentrations of Cr^{3+}. Structural analysis was performed by X-ray diffraction and scanning electron microscopy. Thermogravimetric analysis was performed. Photoacoustic and photoluminescence spectroscopies were employed to characterize the optical properties of the samples and prove the quality of the samples and the right doping.

2 Materials and methods

Cr^{3+}-doped Al_2O_3 (with 0.5, 1.0 and 2.0 Cr^{3+} wt%) samples were prepared by a modified sol–gel method as described previously [34]. Briefly, aqueous diluted PVA (10% w/v) and saturated metal nitrate solutions ($Al(NO_3)_2 \cdot 9H_2O$) and ($Cr(NO_3)_3 \cdot 9H_2O$) were prepared separately and then mixed at certain metal monomer unit ratios. The proportion of Cr^{3+} in the samples were calculated from $Al_{2-x}Cr_xO_3$ stoichiometric formula, where $x = 0.01, 0.02, 0.04$. Analytical-grade reagents were used without further purification. The main function of the polymer in the reaction is to provide a polymeric network to obstruct cations motion, allowing local stoichiometry to be preserved and reducing precipitation of other spurious phases. The solution was maintained at 70 °C under stirring for 2 h and then dried in freeze-dryer. Afterward, the samples were heated up to 200 °C in air atmosphere for 2 h. This is the precursor powder. Subsequently, the powder was placed in an alumina crucible for thermal treatment in air furnace between 600 and 1150 °C for 1 h. The sample treated at 1000 °C showed a light green color, and the samples treated at 1150 °C presented a light red color.

All the Cr^{3+}-doped samples were systematically characterized using various instruments. X-ray powder diffraction

(XRD) data were obtained at room temperature using a X-ray diffractometer (Shimadzu XRD-7000) with Cu-K α radiation ($\lambda = 1.54056$Å). The data were collected in the $20° < 2\theta < 110°$ range in a Bragg–Brentano geometry. For the data obtained from the samples treated at 1150 °C, the structure pattern was refined by the Rietveld method for the identification of the space group and lattice parameters. The precursor powders were analyzed by thermogravimetric analysis (TGA, Netzsch STA 409 PC/PG). This was performed under air atmosphere at a rate of 10 °C min^{-1} from room temperature up to 1000 °C. Gold-coated powders were observed using a scanning electron microscope (SEM) (Shimadzu SSX-550 Superscan).

UV–Vis spectroscopy of the powder sample treated at 1150 °C was obtained using a photoacoustic spectrometer (PAS) as described in detail in Refs. [35–37]. PAS is a remote and nondestructive technique capable of measuring thermal and spectroscopic properties of solids, liquids and gases, with minimum sample preparation [36–40]. A 1000 *W* xenon arc lamp (Oriel Corporation 6269) was used as light source. A monochromator (Oriel Corporation 77250) is coupled to the lamp to separate UV and visible light wavelengths (Oriel, model 77296). The diffracted light is modulated by a mechanical chopper (Stanford Research Systems, model SR 540) and focused on the photoacoustic cell. The photoacoustic signal was detected by a microphone (Brüel and Kjaer 2669) coupled on the photoacoustic cell and to a lock-in amplifier (EG & G Instruments, model 5110). Photoacoustic spectra were obtained at room temperature in the wavelength range of 250 to 800 nm at a modulation frequency of 23 Hz . The samples spectra were normalized by a photoacoustic signal obtained from a carbon black powder.

The photoluminescent (PL) spectra of the samples were obtained exciting the samples with a solid-state laser (Coherent, Verdi 2G) operating at 532 nm. The PL spectrum of each sample was collected by an optical fiber coupled to a linear array spectrometer (Horiba Jobin Yvon, model VS 140) connected to a microcomputer. The PL spectrum is the average from 10 measurements. All the spectra were normalized to 1 in relation to the maximum emission peak. The PL excitation spectrum was obtained using a fluorescence spectrometer (PerkinElmer, model LS 45), at a fixed emission wavelength of 694 nm. All the PL experiments were performed at room temperature. PL lifetime for the emission at 694 nm also was investigated. The same solid-state laser was used as the pump source. A mechanical shutter (SRS, model SR475) was used to modulate the pump laser. The emission of samples was collected by an optical fiber, and the wavelength was selected by a monochromator (Oriel Corporation 77250) assembled with a diffraction array (Oriel, model 77296). The radiative decay lifetime signal was amplified by a photomultiplier tube (Hamamatsu, model R928) biased with a high-voltage power supply (Newport, model 70706) and then collected by a digital oscilloscope (Tektronix, model DPO 4102B), triggered by a photodiode (Thorlabs, PDA10).

3 Results and discussion

TGA curve of the aluminum oxide sample synthesized shows only two weight losses, as presented in Fig. 1. The first weight loss, from room temperature to about 160 °C, corresponds to water evaporation. The second, from 160 to 550 °C, occurs from decomposition of organic materials and the formation of the alumina phase. Above 556 °C, the mass remains constant. The thermogravimetric curve is shown only up to 1000 °C, because no weight loss is associated with the change from gamma to alpha phase [41].

The XRD patterns for alumina doped with 1.0 Cr^{3+} wt% treated between 600 and 1150 °C are presented in Fig. 2. None of the peaks from alumina were observed in the samples treated at 600 °C, suggesting its amorphous nature. The samples treated between 700 and 1000 °C presented peaks at $2\theta = 37.55$, 39.54, 45.97 and 67.05°. All these diffraction peaks could be indexed to the cubic structure of γ-Al_2O_3 (JCPDS: 00-010-0425), which correspond to the (311), (222), (400) and (440) planes. Differently from the samples treated at temperatures up to 1000 °C, which present broad peaks, the sample treated at 1150 °C shows fine and well-defined diffraction peaks and in different positions, which indicates a phase change. The XRD pattern of the sample treated at 1150 °C is in good agreement with the reference XRD pattern of α-Al_2O_3 (42-1468 JCPDS). The sample treated at 1000 °C presents low-intensity

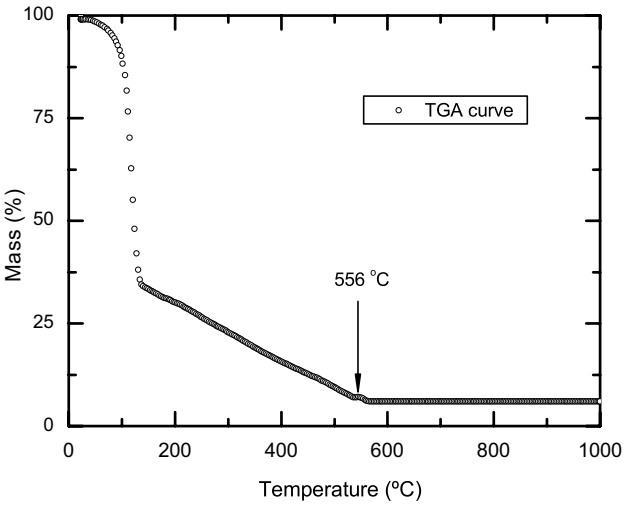

Fig. 1 TGA curve for the α-Al_2O_3 powders. The increase in temperature rate was set up to 10 °C min^{-1}

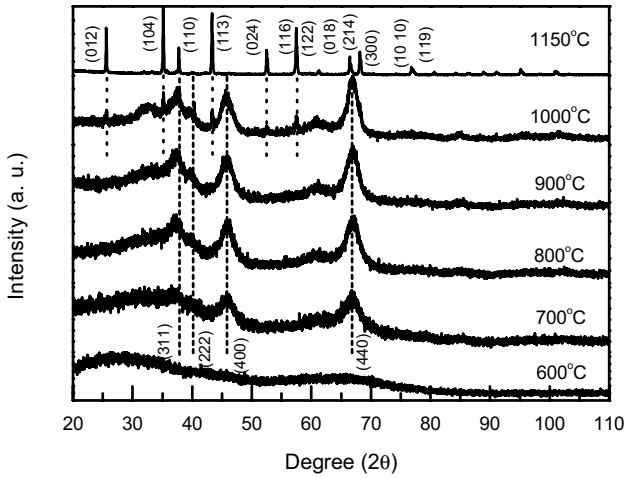

Fig. 2 XRD patterns of α-Al_2O_3 with 1.0 Cr^{3+} wt% annealed at different temperatures

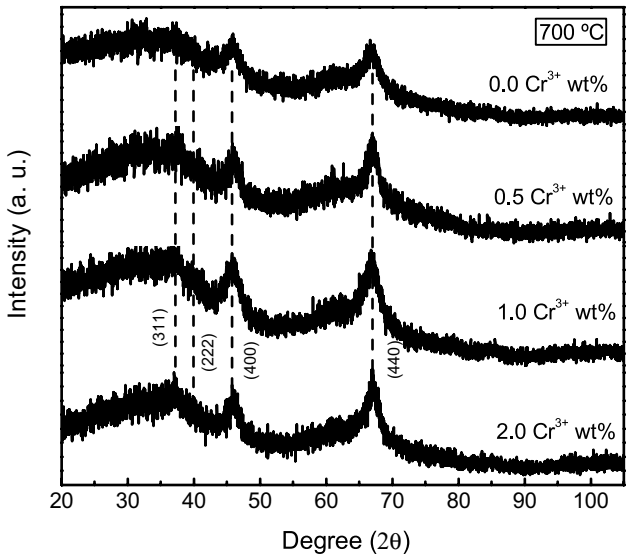

Fig. 3 XRD patterns for Al_2O_3 powders doped with 2.0, 1.0 and 0.5 Cr^{3+} wt%, treated at 700 °C

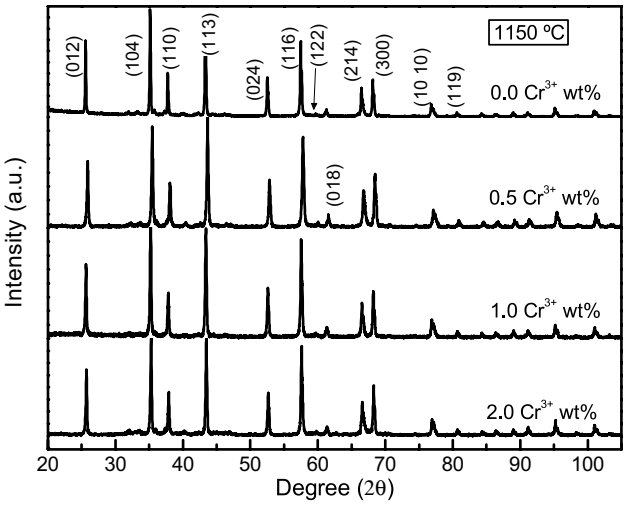

Fig. 4 XRD patterns for Al_2O_3 powders doped with 2.0, 1.0 and 0.5 Cr^{3+} wt%, treated at 1150 °C

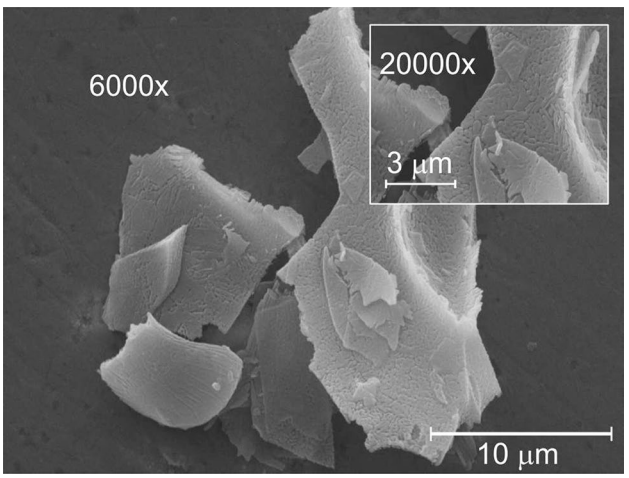

Fig. 5 Scanning electron micrographs for Al_2O_3 powders treated at 1150 °C with magnification of 6000×. Inset shows details with magnification of 20000×

peaks of γ-Al_2O_3. These results are in agreement with TGA measurements.

Figures 3 and 4 show the XRD patterns for samples with different chromium concentrations of 0, 0.05, 1.0 and 2.0 of Cr^{3+} wt% prepared at temperatures of 700 °C and 1150 °C, respectively. The results show the same behavior as the observed for the sample doped with 1.0 Cr^{3+} wt%. The samples treated at 700 °C (Fig. 3) could be indexed as cubic structure of γ-Al_2O_3, and the samples treated at 1150 °C (Fig. 4) could be indexed as α-Al_2O_3. No other predominant phases were observed. In brief, the diffractograms reveal the purity and uniformity of the samples. The morphology of α-Cr^{3+}:Al_2O_3 with 1.0 Cr^{3+} wt% prepared by the sol–gel method treated at 1150 °C was investigated by SEM. Figure 5 shows the SEM images of Cr^{3+}:Al_2O_3 under different resolutions. SEM micrographs show slabs with thickness below 1 μm. The slabs are formed by interconnected long grains of typical thickness of around 200 nm, showing growth of the grains. The size of the grains explains the fine lines observed in the X-ray diffraction experiment. Normalized photoacoustic spectra of Cr^{3+}:Al_2O_3 are shown in Fig. 6. Absorption bands are observed between 312 and 470 nm and between 480 and 600 nm. These bands are very close to those characteristic absorption bands of

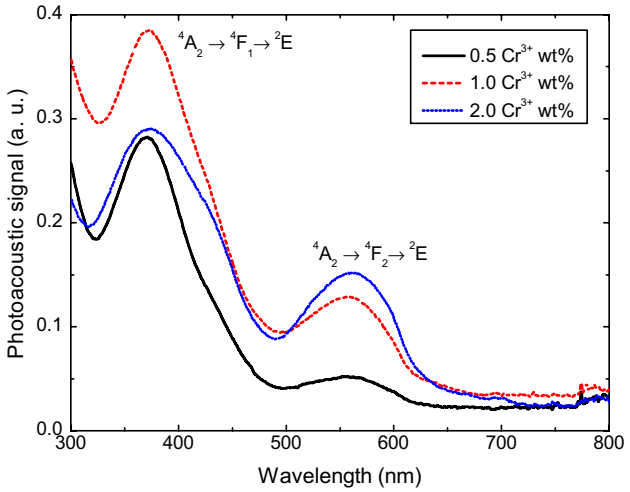

Fig. 6 Normalized photoacoustic spectra of Cr^{3+}:Al_2O_3 powders

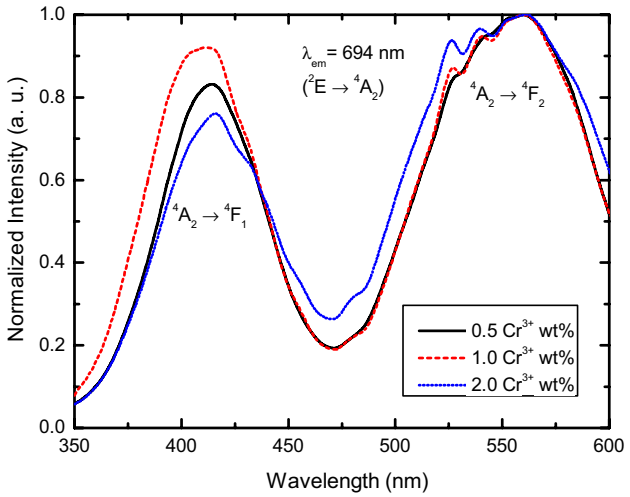

Fig. 7 Normalized PL intensity spectra of Cr^{3+}:Al_2O_3 at a fixed emission, $\lambda_{em} = 694$ λ_{em} = as a function of excitation wavelength

Cr^{3+} obtained from UV–Vis absorption of ruby [20–22] and can be related to the $^4A_2 \rightarrow {}^4F_1$ (violet/blue) and $^4A_2 \rightarrow {}^4F_2$ (green/yellow) transitions [16, 20, 22].

The photoacoustic signal of Cr^{3+}:Al_2O_3 can be related to the non-radiative transitions $^4F_1 \rightarrow {}^2E$ and $^4F_2 \rightarrow {}^2E$ [16, 17]. These transitions convert extra excitation energy into heat in the sample. Since the transition $^4F_1 \rightarrow {}^2E$ has a higher-energy band gap than the $^4F_2 \rightarrow {}^2E$, the photoacoustic signal is larger in the violet region, suggesting a lower heating process when the Cr^{3+}:Al_2O_3 is excited in the green region.

Figure 7 shows the normalized PL intensity spectra of Cr^{3+}:Al_2O_3 at a fixed emission at 694 nm as a function of excitation wavelength. A emission at 694 nm is observed when the sample is excited at 360-470 nm and 490-625 nm bands, indicating the existence of the transitions $^4A_2 \rightarrow {}^4F_1$ and $^4A_2 \rightarrow {}^4F_2$. This results from the $^4F_1 \rightarrow {}^2E$ and $^4F_2 \rightarrow {}^2E$ transitions observed in the photoacoustic signal and to the $^2E \rightarrow {}^4A_2$ transitions from the PL (Fig. 8). A slight change in intensity of luminescence in comparison with a maximum normalized at the transition $^4A_2 \rightarrow {}^4F_1$ was observed for all samples. The PL spectra of Cr^{3+}:Al_2O_3, related to the $^2E \rightarrow {}^4A_2$ transition also, were investigated, as shown in Fig. 8, obtained for Cr^{3+}:Al_2O_3 samples excited at 532 nm. The $^2E \rightarrow {}^4A_2$ transition maximum emission was obtained at 694 nm, showing that the maximum emission is in good agreement with the literature for ruby R lines [17, 20, 22]. A decrease in PL intensity at R line when compared to the 700–800 nm emission was observed as a function of the increase in Cr^{3+} concentration, especially for 2.0 wt% Cr^{3+} sample. A maximum R line emission would be expected for samples with 0.3–0.5 wt% Cr^{3+}, as previously reported by Lapraz et al. [18]

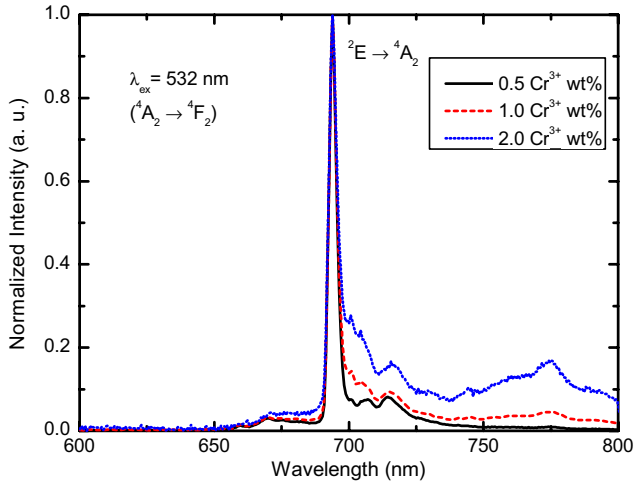

Fig. 8 Normalized PL spectra of Cr^{3+}:Al_2O_3 with a excitation wavelength $\lambda_{ex} = 532$ nm

Figure 9a shows the PL lifetime of the samples as a function of Cr^{3+} concentration. PL lifetime of $^2E \rightarrow {}^4A_2$ transition experimental curves showed a non-exponential behavior. The experimental data were fitted to the equation [42–44]

$$I(t) = I_0 + A_1 e^{-\frac{t}{\tau_1}} + A_2 e^{-\frac{t}{\tau_2}} \quad (1)$$

where $I(t)$ is the PL intensity at a time t, I_0 is the PL at $t = 0$, τ_1 is the fast and τ_2 is the slow decay components. A_1 and A_2 are the amplitude related to each decay components [43]. The average lifetimes were calculated using the relation [43, 44]

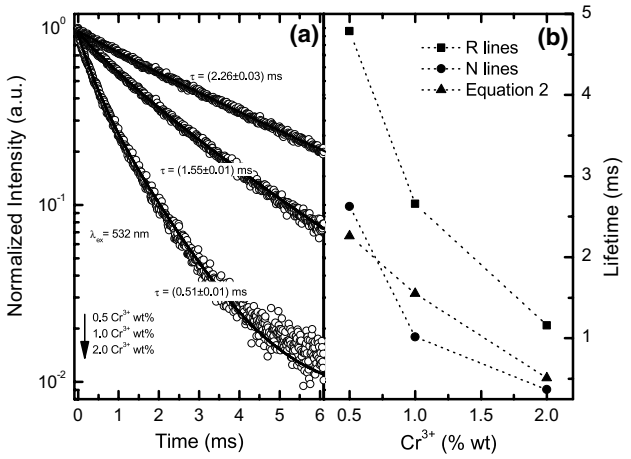

Fig. 9 **a** Normalized PL lifetimes curve of Cr^{3+}:Al_2O_3-doped powders at R and N lines when excited with $\lambda_{ex} = 532$ nm. Circles are experimental data and solid lines are fitted curves (Eq. 1); **b** fast, slow and mean (Eq. 2) lifetime decay components: Fast decay times are related to N lines and slow decay times are related to R lines

$$\langle \tau \rangle = \frac{(A_1\tau_1)^2 + (A_2\tau_2)^2}{(A_1\tau_1) + (A_2\tau_2)} \quad (2)$$

For ruby, the long decay time related to the single chromium ion emission and the fast decay time related to the pairs and four paired ions (Nlines) [45, 46] are shown in Figure 9b. Since our samples are in relatively high chromium concentration, an increase in the number of pairs is also observed [45, 46]. The values obtained are shown in the figure and a decrease in the lifetime is observed, suggesting a quenching process accordingly to data reported by *Birgeneau* [19]. That explains the decrease in 694 nm intensity of PL.

4 Conclusion

We have proposed a low-cost and simple modified sol–gel method to synthesize Cr^{3+}:Al_2O_3. The Rietveld analysis based on X-ray diffraction data showed that the space group and lattice parameters are in agreement with Cr^{3+}:Al_2O_3 data and a single phase was obtained. Photoacoustic spectroscopy allowed to observe the absorption bands in the violet/blue and green/yellow ranges, which is in good agreement with those reported for ruby crystal. Photoluminescence was detected and a maximum peak was obtained at 694 nm for all samples. Photoluminescence was found to depend directly on the chromium concentration, showing a decrease in the ratio between the R line peak and the 700–800 nm emission band with the increase in dopant concentration. The influence of chromium concentration also can be observed on the lifetime decay at 694 nm. The mean lifetime decay decreases as a function of the increasing chromium concentration. The results of photoacoustic spectroscopy and photoluminescence are in agreement with the literature, which proves that the chrome stoichiometry was maintained, with no loss of chromium during the manufacturing process. The sol–gel method presented here is simple and allows for an easy way to manufacture thin films by spin coating. Considering its easy and low-cost preparation, Cr^{3+}:Al_2O_3 reveals as an alternative product in application for cooling down environments due its luminescent properties in addition to other applications.

Acknowledgements The authors acknowledge the support from the Brazilian agencies CAPES, CNPq, Fundação Araucária and FINEP.

Compliance with ethical standards

Conflict of interest On behalf of all authors, the corresponding author states that there is no conflict of interest.

References

1. Rahman AZMS (2016) Solid state luminescent materials: applications. In: Hashmi S (ed) Reference module in materials science and materials engineering. Elsevier, Amsterdam
2. Merigeon J, Maalej O, Boulard B, Stanculescu A, Leontie L, Mardare D, Girtan M (2015) Studies on Pr^{3+}-Yb^{3+} codoped ZBLA as rare earth down convertor glasses for solar cells encapsulation. Opt Mater 48:243–246
3. Miniscalco WJ (1991) Erbium-doped glasses for fiber amplifiers at 1500 nm. J Lightwave Technol 9:234–250
4. Mori A, Ohishi Y, Sudo S (1997) Erbium-doped tellurite glass fibre laser and amplifier. Electron Lett 33:10–11
5. Fujimoto Y, Nakatsuka M (2003) Optical amplification in bismuth-doped silica glass. Appl Phys Lett 82:3325
6. Yang J, Dai S, Zhou Y, Wen L, Hu L, Jiang Z (2003) Spectroscopic properties and thermal stability of erbium-doped bismuth-based glass for optical amplifier. J Appl Phys 93:977
7. Peng M, Wu B, Wang C, Zhu C, Qiu J, Chen D (2008) Bismuth-activated luminescent materials for broadband optical amplifier in WDM system. J Non Cryst Solids 354:1221–1225
8. Duffy JF, Czeisler CA (2009) Effect of light on human circardian physiology. Sleep Med Clin 4:165–177
9. LeGates TA, Fernandez DC, Hattar S (2014) Light as a central modulator of circadian rhythms, sleep and affect. Nat Rev Neurosci 15:443–454
10. Zak PP, Lapina VA, Pavich TA, Trofimov AV, Trofimova NN, Tsaplev YB (2017) Luminescent materials for modern light sources. Russ Chem Rev 86:831–844
11. Synnefa A, Santamouris M, Apostolakis K (2007) On the development, optical properties and thermal performance of cool colored coatings for the urban environment Sol. Energy 81:488–497
12. Levinson RM, Akbari H, Reilly JC (2007) Cooler tile-roofed buildings with near-infrared-reflective non-white coatings. Build Environ 42:2591–2605

13. Kolokotsa D, Maravelaki-Kalaitzaki P, Papantoniou S, Vangeloglou E, Saliari M, Karlessi T, Santamouris M (2012) Development and analysis of mineral based coatings for buildings and urban structures. Sol Energy 86:1648–1659
14. Takebayashi H, Moriyama M, Sugihara T (2012) Study on the cool roof effect of Japanese conventional tiled roof: numerical analysis of solar reflectance of unevenness tiled surface and heat budget of typical tiled roof system. Energy Build 55:77–84
15. Berdahl P, Chen SS, Destaillats H, Kirchstetter TW, Levinson RM, Zalich MA (2016) Fluorescent cooling of objects exposed to sunlight—the ruby example. Sol Energy Mater Sol Cells 157:312–317
16. Maiman TH (1960) Optical and microwave-optical experiments in ruby. Phys Rev Lett 4:564–566
17. Maiman TH (1960) Stimulated optical radiation in ruby. Nature 187:493–494
18. Lapraz D, Iacconi P, Daviller D, Guilhot B (1991) Thermostimulated luminescence and fluorescence of α-Al_2O_3 samples (Ruby). Influence of the Cr^{3+} concentration. Phys Status Solidi (a) 126:521–531
19. Birgeneau RJ (1969) Mechanisms of energy transport in ruby. J Chem Phys 50:4282
20. Penilla EH, Hardin CL, Kodera Y, Basun SA, Evans DR, Garay JE (2016) The role of scattering and absorption on the optical properties of birefringent polycrystalline ceramics: modeling and experiments on ruby (Cr:Al_2O_3). J Appl Phys 119:23106
21. Cronemeyer DC (1966) Optical absorption characteristics of pink ruby. J Opt Soc Am 56:1703–1706
22. Esposti CD, Bizzocchi L (2007) Absorption and emission spectroscopy of a lasing material: ruby. J Chem Educ 84:1316–1318
23. Piermarini GJ, Block S (1975) Ultrahigh pressure diamond-anvil cell and several semiconductor phase transition pressures in relation to the fixed point pressure scale. Rev Sci Instrum 46:973
24. Muniz RF, De Ligny D, Martinet C, Sandrini M, Medina AN, Rohling JH, Baesso ML, Lima SM, Andrade LHC, Guyot Y (2016) In situ structural analysis of calcium aluminosilicate glasses under high pressure. J Phys Condens Matter 28:315402
25. Nguyen DK, Lee H, Kim IT (2017) Synthesis and thermochromic properties of Cr-doped Al_2O_3 for a reversible thermochromic sensor. Materials 10:476
26. Zhu Y-L, Liu S, Zhang X-K, Xiang Y (2018) Effects of Cr^{3+} concentration on the crystallinity and optical properties of Cr-doped Al_2O_3 powders by solid-state reaction method. IOP Conf Ser Mater Sci Eng 382:22037
27. Liu Q, Yang QH, Zhao GG, Lu SZ, Zhang HJ (2013) The thermoluminescence and optically stimulated luminescence properties of Cr-doped alpha alumina transparent ceramics. J Alloys Compd 579:259–262
28. Danks AE, Hall SR, Schnepp Z (2016) The evolution of sol–gel chemistry as a technique for materials synthesis. Mater Horiz 3:91–112
29. Patra A, Tallman RE, Weinstein BA (2005) Effect of crystal structure and dopant concentration on the luminescence of Cr^{3+} in Al_2O_3 nanocrystals. Opt Mater 27:1396–1401
30. Ardizzone S, Bianchi CL, Galassi C (2000) Chromium doped γ-Al_2O_3 powders. Features of the electrical double layer and state of the surface species. J Organomet Chem 490:48–53
31. Fujita K, Tokudome Y, Nakanishi K, Miura K, Hirao K (2008) Cr^{3+}doped macroporous Al_2O_3 monoliths prepared by the metal-salt-derived sol–gel method. J Non-Cryst Solids 354:659–664
32. Salek G, Devoti A, Lataste E, Demourgues A, Garcia A, Jubera V, Gaudon M (2016) Optical properties versus temperature of Cr-doped γ- and α-Al_2O_3: irreversible thermal sensors application. J Lumin 179:189–196
33. Nguyen DK, Bach Q-V, Kim B, Lee H, Kang C, Kim I-T (2019) Synthesis of Cr-doped Al_2O_3 by Pechini sol–gel method and its application for reversible thermochromic sensors. Mater Chem Phys 223:708–714
34. Ciciliati MA, Silva MF, Fernandes DM, De Melo MAC, Hechenleitner AAW, Pineda EAG (2015) Fe-doped ZnO nanoparticles: synthesis by a modified sol–gel method and characterization. Mater Lett 159:84–86
35. Ames FQ, De Arruda LLM, Rocha BA, Cuman RKN, Bersani-amado CA, Sato F, De Castro LV, De Arruda LLM, Rocha BA (2017) Evidence of anti-inflammatory effect and percutaneous penetration of a topically applied fish oil preparation: a photoacoustic spectroscopy study. J Biomed Opt 22:55003
36. Somer A, Camilotti JG, Gonalves A, Bonardi C, Cruz GK, Beltrame FL, Sato F, Astrath NGC, Novatski A (2015) Polyvinylpyrrolidone quantification in paracetamol using phase-resolved photoacoustic method. Spectrosc Lett 48:427–430
37. Coelho TM, Vidotti EC, Rollemberg MC, Medina AN, Baesso ML, Cella N, Bento AC (2010) Photoacoustic spectroscopy as a tool for determination of food dyes: comparison with first derivative spectrophotometry. Talanta 81:202–207
38. West GA, Barrett JJ, Siebert DR, Reddy KV (1983) Photoacoustic spectroscopy. Rev Sci Instrum 54:797–817
39. Monchalin J-P, Bertrand L, Rousset G, Lepoutre F (1984) Photoacoustic spectroscopy of thick powdered or porous samples at low frequency. J Appl Phys 56:190–210
40. Miklós A, Hess P, Bozki Z (2001) Application of acoustic resonators in photoacoustic trace gas analysis and metrology. Rev Sci Instrum 72:1937–1955
41. Lamouri S, Hamidouche M, Bouaouadja N, Belhouchet H, Garnier V, Fantozzi G, Franc J (2017) Control of the γ-alumina to α-alumina phase transformation for an optimized alumina densification. Bol La Soc Española Cerámica Y Vidr 56:47–54
42. Knutson JR, Beechem JM, Brand L (1983) Simultaneous analysis of multiple fluorescence decay curves: a global approach. Chem Phys Lett 102:501–507
43. Naresh V, Ham BS (2016) Influence of multiphonon and cross relaxations on $^3P_0$ and $^1D_2$ emission levels of Pr^{3+} doped borosilicate glasses for broad band signal amplification. J Alloys Compd 664:321–330
44. Ma S, Feng W, Chen R, Peng Z (2017) $KSr_4(BO_3)_3$:Pr^{3+}: a new red-emitting phosphor for blue-pumped white light-emitting diodes. J Alloys Compd 700:49–53
45. Schawlow AL, Wood DL, Clogston AM (1959) Electronic spectra of exchange-coupled ion pairs in crystals. Phys Rev Lett 3:271–273
46. Imbusch GF (1967) Energy transfer in ruby. Phys Rev 153:326–337